International Society for Biofabrication

PURPOSE-LED PUBLISHING™

PAPER

High-resolution bioprinting of complex bio-structures via engineering of the photopatterning approaches and adaptive segmentation

To cite this article: Ceren Babayigit *et al* 2025 *Biofabrication* **17** 025026

View the article online for updates and enhancements.

PAPER

High-resolution bioprinting of complex bio-structures via engineering of the photopatterning approaches and adaptive segmentation

Ceren Babayigit[1,4], Jorge Alfonso Tavares-Negrete[2,4] , Rahim Esfandyarpour[1,2,3,*] and Ozdal Boyraz[1,*]

[1] Department of Electrical Engineering and Computer Science at the University of California, Irvine, CA 92697, United States of America
[2] Department of Biomedical Engineering at the University of California, Irvine, CA 92697, United States of America
[3] Department of Mechanical and Aerospace Engineering at the University of California, Irvine, CA 92697, United States of America
[4] Equal contribution.
* Authors to whom any correspondence should be addressed.

E-mail: rahimes@uci.edu and oboyraz@uci.edu

Abstract

Digital light processing (DLP) technology has significantly advanced various applications, including 3D bioprinting, through its precision and speed in creating detailed structures. While traditional DLP systems rely on light-emitting diodes (LEDs), their limited power spectral density, high etendue, and spectral inefficiency constrain their performance in resolution, dynamic range, printing time, and cell viability. This study proposes and evaluates a dual-laser DLP system to overcome these limitations and enhance bioprinting performance. The proposed dual-laser system resulted in a twofold increase in resolution and a twelvefold reduction in printing time compared to the LED system. The system's capability was evaluated by printing three distinct designs, achieving a maximum percentage error of 1.16% and a minimum of 0.02% in accurately reproducing complex structures. Further, the impact of exposure times (10–30 s) and light intensities (0.044–0.11 mW mm^{-2}) on the viability and morphology of 3T3 fibroblasts in GelMA and GelMA-poly(ethylene glycol) diacrylate (PEGDA) hydrogels is assessed. The findings reveal a clear relationship between longer exposure times and reduced cell viability. On day 7, samples exposed for extended periods exhibited the lowest metabolic activity and cell density, with differences of ∼40% between treatments. However, all samples show recovery by day 7, with GelMA samples exhibiting up to a sixfold increase in metabolic activity and GelMA-PEGDA samples showing up to a twofold increase. In contrast, light intensity variations had a lesser effect, with a maximum variation of 15% in cell viability. We introduced a segmented printing method to mitigate over-crosslinking and enhance the dynamic range, utilizing an adaptive segmentation control strategy. This method, demonstrated by printing a bronchial model with a 14.43x compression ratio, improved resolution and maintained cell viability up to 90% for GelMA and 85% for GelMA-PEGDA during 7 d of culture. The proposed dual-laser system and adaptive segmentation method were confirmed through successful prints with diverse bio-inks and complex structures, underscoring its advantages over traditional LED systems in advancing 3D bioprinting.

1. Introduction

Digital light processing (DLP) technology has revolutionized various fields such as 3D bioprinting [1, 2], projection systems [3], medical imaging [4], and various advanced optical applications [5, 6] due to its precision, versatility, and speed in creating intricate structures. Especially, the integration of DLP into 3D bioprinting as light-driven technology has shown significant promise for medical and bioengineering applications, enabling the creation of complex biological structures with high precision and facilitating

the use of a variety of bioinks. For example, Grigoryan *et al* [7] developed a vascularized alveolar model replicating intricate micro vessel networks, accurately simulating blood flow and oxygen delivery in response to cyclic alveolar motions. In another study, a liver-on-a-chip platform was developed using DLP bioprinting, incorporating perfusion-enabled channel systems for nutritional supply and containing cell-laden tissue within GelMA bioink, with twelve channels running from the model edges to a central port [8].

The DLP printing process is essentially a photochemical synthesis mechanism, wherein a light source serves as the primary energy input that is dynamically controlled by digital micromirrors device (DMD), a mechanical printing platform functions as the reaction container, and photo-curable precursors act as the reactive mixtures (see figure 1(a)). This mechanism operates by projecting a light pattern onto a photopolymer resin layer, causing the illuminated regions to solidify while leaving the rest in a liquid state. The core of this technology is the DMD, which consists of an array of tiny mirrors that can tilt to reflect light in a specific pattern [9]. By controlling the tilt of each micromirror, the DLP system can dynamically shape the light to match the desired cross-sectional pattern of the 3D model being printed. As each layer is exposed to the light, the resin hardens and the build platform moves incrementally to allow successive layers to be cured on top of each other, building up the final 3D structure layer by layer. This layer-by-layer construction enables the creation of highly detailed and complex structures with fine-resolution [10, 11]. Using photo-curable resins, which polymerize when exposed to specific wavelengths of light, ensures that the printed structures are solid and stable. This process is not only precise but also relatively fast, making DLP a preferred method for applications requiring high detail and accuracy, such as in the fields of bioengineering and medical modeling [12, 13].

The quality and efficiency of DLP bioprinting are influenced by several interrelated factors, including the characteristics of the light source (wavelength, intensity, and exposure time), the composition and properties of the photoinitiators and resins, and the specific printing parameters (layer thickness, resolution, and print speed). Among these factors, the selection and optimization of the light source play a crucial role in fully harnessing the potential of the bioprinting process. Traditionally, DLP systems have relied on light-emitting diodes (LEDs) due to their availability and cost-effectiveness. However, while LEDs have facilitated significant advancements, there remain areas for improvement. Specifically, they are limited to low output power and power spectral density, resulting in slower polymerization and correspondingly longer build times [14]. Printing time is crucial especially for bioprinting and cell viability because

extending it can lead to cellular stress or damage, thereby compromising the integrity and functionality of the printed biostructures [15]. Hence, reducing build times is crucial to maintaining higher cell viability and ensuring the bio-printed structures retain their intended biological functions. Additionally, the capabilities of these systems are constrained by the principle of étendue, creating an inherent trade-off between brightness and contrast ratio [16]. High étendue significantly impacts the printing process and outcomes by reducing light intensity, dynamic range of the system, and resolution. This constraint leads to increased printing times and diminishes the resolution, precision, and structural integrity of printed biostructure by blurring fine details and compromising layer adhesion [17]. Consequently, the efficiency and quality of the bioprinted structures are adversely affected, potentially hindering their functional and mechanical properties. Also, LEDs can produce light with any color, but at a wide spectral width of about 5% of the central wavelength, resulting in lower absorption efficiency by the photoinitiators [18]. This inefficiency means that a greater portion of the emitted light is not effectively utilized for polymerization, leading to longer exposure times, reduced curing efficiency, and increased risk of phototoxicity.

Laser sources can be employed to address these constraints. They offer high output power and precise frequency that matches the absorption line of photoinitiators [19, 20]. Hence, it allows for rapid and efficient photopolymerization of bioinks, speeding up the printing process and enabling the fabrication of complex structures with greater precision [14]. Moreover, the narrow spectral bandwidth of lasers ensures precise wavelength emission, enhancing the accuracy of photopolymerization and minimizing unintended exposure that could harm biological materials. Additionally, laser sources exhibit favorable étendue characteristics, enabling the efficient transfer of optical power while maintaining spatial and angular distributions. Also, their small étendue minimizes the light divergence and blurring of light, thereby enhancing both the resolution and the dynamic range of the system [21]. More importantly, the small size of a laser's étendue allows for the easy combination of multiple laser sources without any light losses [16]. Therefore, the versatile capabilities of laser sources, encompassing output power, étendue characteristics, and spectral precision, render them indispensable tools in various optical applications, including advanced printing technologies and biomedical research.

In this work, we present a cutting-edge DLP bioprinting technique designed to enable high-resolution biofabrication of complex 3D organ structures with living cells. Our approach addresses the challenges of printing intricate biological structures with precision, particularly those involving dense,

multilayered tissue architectures. The goal is to show how to enhance print resolution and dynamic range ($\frac{\text{Max printing area}}{\text{Min Feature Size}}$), reduce exposure times while maintaining throughput, as well as preserving a cell-friendly printing process when working with biomaterials. The proposed system represents a significant advancement in the field of 3D bioprinting, overcoming the limitations of traditional LED-based systems by offering superior resolution, dynamic range, and printing speed. Another critical aspect of this laser-based technique is the development of an adaptive segmentation method to optimize the photopolymerization process to address dynamic range challenges that limit resolution in large biostructures. As part of this work, we systematically compared the performance of our laser-based system with conventional LED-based setups, demonstrating clear advantages in print quality and operational efficiency. We also show a dual-laser system for illumination implementation that results in a reduction of speckle contrast by a factor of $1/\sqrt{2}$, and a twofold increase in resolution for the same source intensity. Additionally, we show that for the same source intensity and feature size, the printing time was reduced by a factor of 12. The system's capability to print complex structures was evaluated by printing three distinct designs and conducting registration analyses. These analyses revealed that the system achieved a maximum percentage error of 1.16% and a minimum of 0.02% in accurately reproducing these structures. Additionally, we assessed how exposure times (10–30 s) and light intensities (0.044–0.11 mW mm^{-2}) in a laser-based bioprinter affect the viability and morphology of 3T3 fibroblasts in GelMA and GelMA-poly(ethylene glycol) diacrylate (PEGDA) hydrogels. Between 10 and 30 s of crosslinking, cell viability decreases by approximately 47.59% for GelMA and 32.60% for GelMA-PEGDA. However, all samples show recovery by day 7, with GelMA samples exhibiting up to a sixfold increase in metabolic activity and GelMA-PEGDA samples showing up to a twofold increase. Cells in the 10 second crosslinked samples recover faster than those in the 20- and 30 s samples. In contrast, varying light intensities had a lesser impact on cell viability, showing a maximum variation of 15% across the tested range. It is systematically demonstrated that by increasing the light intensity, we can enhance the system's resolution and further decrease the crosslinking time while maintaining the cell viability. To address over-crosslinking in large, dense, intricate models, we introduce an adaptive segmentation control method. This technique segments the photomask into discrete regions and uses an on-off activation strategy to manage the distribution and concentration of free radicals. By strategically alternating activation between segments, the method reduces over-crosslinking and improves resolution. Demonstrated by printing a bronchial model with a 100 μm gap between branches at a 14.43x compression ratio to

anatomical size, this technique has shown improved resolution and maintained cell viability up to 90% for GelMA and 85% for GelMA-PEGDA constructs across seven days. This segmentation method also supports enhanced dynamic range, crucial for achieving high resolution and fidelity in complex prints. Through this systematic and detailed comparative study, we aim to establish the benefits and potential applications of a laser-based DLP bioprinting system, offering insights into its superiority over traditional LED-based systems in terms of resolution, printing speed, dynamic range, and material compatibility, thereby advancing the field of 3D bioprinting.

2. Materials and methods

2.1. Materials

PEGDA-700 Mn 700 (26570-48-9) and quinoline yellow (QY) (8004-92-0) were purchased from Sigma Aldrich, USA. Lithium phenyl-2,4,6- trimethylbenzoyl phosphinate (LAP) was purchased from TETHON, USA. Dulbecco's Modified Eagle Medium (DMEM) media (11965-092), ANTI-ANTI (15240-062), Trypsin-EDTA (25200-072) and fetal bovine serum (A52094-01) were purchased from Gibco, USA. Resazurin assay (AR002) was purchased from R&D Systems, USA. NIH-3T3 fibroblasts were purchased from ATCC, USA. LIVE/DEAD assay (R37601) and Phaloidin ActinGreen 488 (R377110) were purchased from Invitrogen, USA. The ultraviolet (UV)-395 nm torch and lasers were purchased from Darkbeam-Amazon. DLP Projector (DLP Light Commander) was purchased from Texas Instruments, USA. Lenses, iris, and mirrors were purchased from Thorlabs.

2.2. GelMA synthesis

GelMA ∼90% Degree of substitution grade was synthesized following our previous protocol [22] by dissolving type A gelatin from porcine skin at 10% (w/v) in Dulbecco's phosphate-buffered saline solution (DPBS) and stirring at 50 °C and 600 rpm for 1 h. Methacrylic anhydride was added dropwise with a syringe pump (0.25 ml min^{-1}) to the solution at 10% (v/v) and allowed to react for 1 h. The reaction was stopped by adding 3× volumes of DPBS. Then the solution was dialyzed against distilled water with a cut-off dialysis membrane of 12 kDa for 7 d. The dialyzed solution was frozen and lyophilized for 7 d and then stored at 4 °C for further use [23].

2.3. Preparation of PEGDA ink

For the resolution and 3D model printing, a solution of 15% w/v of PEGDA-700 in distilled water was mixed with 0.1% w/v QY and LAP 0.1% w/v. The solution was heated at 60 °C and stirred at 700 rpm over a hotplate for 1 h.

2.4. Preparation of GelMA ink

Freeze-dried GelMA was dissolved at 7.5% w/v in distilled water and mixed with QY 0.1% w/v and LAP 0.1% w/v. The solution was heated at 60 °C and stirred at 700 rpm over a hotplate for 1 h. The GelMA solutions were sterilized via a syringe filter using 0.22 μm polyether sulfone (PES) filters before being used with cells.

2.5. Preparation of GelMA-PEGDA ink

A PEGDA prepolymer solution of 1% w/v of PEGDA-700, 0.1% w/v of QY, and 0.1% w/v of LAP in distilled water was prepared. The solution was heated at 60 °C and stirred at 700 rpm for 1 h. The PEGDA solutions were sterilized via a syringe filtering using 0.22 μm PES.

The GelMA solution described in section 2.3 was used for the formulation of the GelMA-PEGDA ink as described as follows; A blend of 9:1 of sterile GelMA 7.5% and PEGDA 1% was mixed at 60 °C and stirred at 700 rpm for 1 h.

2.6. DLP printing system with LED source

The system was built by customizing the projection lens and illumination source of a commercial DLP system (Texas Instruments, Dallas, TX). The original visible light illumination module was replaced with an LED UV source at a wavelength of 395 nm and intensity of 0.02 mW mm^{-2} to illuminate the DMD chips. The projection optics were modified by incorporating a 4-*f* optical system by using projection lenses (Thorlabs, Newton, NJ) with 150 mm focal length. The DMD chip (Texas Instruments, Dallas, TX) in the system consists of 1024 × 768 individually controllable micromirrors, each with a size of 10.8 μm. The *z*-axis movement was facilitated by a linear stage (Fuyu Motion, Sichuan, China) and a digital stepper motor driver (Stepperonline, New York, NY). The individual movements of the stage, light source, and DMD mirrors were controlled using an Arduino microcontroller.

2.7. DLP printing system with LASER source

The laser source system was constructed using custom modifications to a commercial DLP system (Texas Instruments, Dallas, TX). To enhance the performance, the original visible light illumination module was substituted with two UV laser sources (Oxlasers, Shanghai, China) operating at 405 nm. Unlike high-power fiber-coupled lasers that require costly drivers [24], our laser modules are cost-effective and operate with a simple 12 V DC power supply, eliminating the need for additional controllers while maintaining stable illumination. Integration of these laser sources is utilized by polarizing beamsplitter cube (Thorlabs, Newton, NJ). To efficiently combine their outputs, the polarization of the second laser is controlled by incorporating a half-wave plate (Thorlabs, Newton, NJ). The intensity of the lasers is dynamically adjusted using adjustable neutral density (ND) filters (Lightdow, Shenzhen, China) which allow precise control over the output power/intensity levels of the system. By using plano-convex lenses with a focal length of 150 mm (Thorlabs, Newton, NJ), the projecting optics have been modified with the 4-*f* system. The DMD chip (Texas Instruments, Dallas, TX) with 1024 × 768 individually controllable micromirrors of 10.8 μm size is used for the mask projection. A linear stage (Fuyu Motion, Sichuan, China) and a digital stepper motor driver (Stepperonline, New York, NY) assisted the *z*-axis movement. Using an Arduino microcontroller, we could control the stage's movements, lighting sources, and DMD mirrors individually.

2.8. Mask preparation

Predefined computer-aided design (CAD) models are sliced into a layer-by-layer structure by MATLAB, resulting in the generation of .bmp files. Subsequent cosmic edits are implemented using Adobe Illustrator and batch files are created by e LOGIC application software.

2.9. Printing resolution evaluation

A calibration structure consisting of an array of strips with decreasing sizes and gaps has been printed to evaluate the print resolution of the system. Image analysis was used to assess the fidelity of printed structures after the recovery of the samples. Photographic images of printed structures have been analyzed using Toupview software (AmScope, USA) and compared to the original design parameters.

2.10. Mask preparation for graded intensity analyses

We have investigated the impact of light intensity modulation on cell behavior by manipulating the DMD to create graded intensity distributions. The DMD area was divided into four equal rectangular regions, each assigned a targeted power level. We calculated the necessary number of mirrors to activate ('on') and deactivate ('off') for each region to achieve the desired intensity levels. Subsequently, we generated masks by randomly distributing on/off mirror states across the respective areas. Maintaining constant exposure time, we printed four distinct regions with varying total light intensities. The diffusion effects facilitated the achievement of fully crosslinked structures, thereby exploring the relationship between controlled light-intensity gradients and cellular responses in bioprinted constructs.

2.11. Cell culture

Mouse 3T3 fibroblast was used for this study. Cells were cultured in an incubator at 37 °C under a 5% CO_2 atmosphere. DMEM supplemented with 10%

fetal bovine serum and 1% Anti-Anti was used as standard cell culture media.

2.12. 3D bioprinting

For the 3D bioprinting experiments, GelMA and GelMA-PEGDA inks were sterilized using a 0.22 μm nylon syringe filter. 3T3 fibroblasts were then trypsinized and dispersed by pipetting into the inks at a concentration of 3×10^6 cells ml^{-1}. The bioprinting process was carried out inside a fume hood, with an air heater used to maintain the process temperature and prevent gelation. Rectangular structures of 1×7.4 mm were printed, consisting of seven layers, each with a thickness of 250 μm.

2.13. Metabolic activity

The metabolic activity of the bioprinted structures was determined using the Resazurin assay (Biotium, USA). Briefly, 3D bioprinted constructs were covered in DMEM culture medium with 10% v/v resazurin reagent and incubated for 2 h at 37 °C. In a 96-well plate, 100 μl of the medium was dispensed, and the fluorescence was measured in a microplate reader (Biotek Cytation 5, USA) at 530/570 nm excitation and emission wavelengths. To facilitate the comparison of the effects of exposure time or light intensity on metabolic activity, samples were normalized relative to the lowest exposure time or light intensity measured (i.e. 10 s or 0.04 mW mm^{-2}) on day 1.

2.14. Cell density

The quantification of cell density as an indicator of cell proliferation was evaluated using brightfield images taken with the microscope and converted to a 16-bit gray value format. The cell numbers were counted excluding cellular debris and apoptotic bodies using a cell counter plugin from Fiji (NIH, USA).

To assess the effect of exposure time on the cell density of independent samples, cell density was calculated as follows:

$$\text{Cell density}_{\text{Exposure time}} = \frac{\text{\# cells in the field of view of the microscope}}{\text{area of the field of view of the microscope}}). \tag{1}$$

For evaluating the effect of light intensity on the cell density of a single structure with four distinct regions having graded intensity distributions cell density was calculated using the formula:

$$\text{Cell density}_{\text{light intensity}} = \frac{\text{\# cells in the field of view of the independent region}}{\text{\# cells in counted in the entire structure}}). \tag{2}$$

2.15. Exposure time analysis

To evaluate the effect of exposure time on cell viability, three exposure times—10 s, 20 s, and 30 s per layer—were tested under consistent experimental conditions. A total of seven layers were printed for each exposure time, with total printing times ranging from 70 s (for 10 s per layer) to 210 s (for 30 s per layer).

2.16. Fluorescent staining and microscopy

The biocompatibility of the laser bioprinting was checked on days 1,3 and 7 using LIVE/DEAD assay, Briefly, samples were washed three times with phosphate-buffered saline (PBS) and treated with the staining solution for 30 min at room temperature, later staining solution was discarded, and the samples were washed with PBS one more time. The assayed samples were processed with a confocal fluorescence microscope (Zeiss, LSM 980 with Airyscan 2/two-photon laser). Maximum intensity projections for the green channel (calcein) and the red channel (propidium iodide) were used to calculate cell viability. Image analysis was conducted using Fiji (NIH, USA). Six images from two independent biological replicates were analyzed. Cell viability is calculated with the following formula:

$$\text{Cell viability } \% = \frac{\text{Number of cells alive}}{\text{Total number of cells}} \times 100. \tag{3}$$

The aspect ratio of 3T3 fibroblasts embedded in the bioinks was calculated by measuring the longer side and the shorter side of the cells. Sixty cells were randomly selected per day per condition for this analysis. The aspect ratio was determined by dividing the longer side by the shorter side.

The cytoskeleton was evaluated using fluorescent staining as follows; The cell-laden structures were fully covered with 4% paraformaldehyde solution in PBS for 30 min at room temperature to fix the cells. Samples were later washed with PBS three times and stained with Palloidin Alexa Fluor 488 (Fisher) for F-actin filaments and 1 μg ml^{-1} of DAPI-PBS for cell nuclei overnight. Later, samples were washed three times with PBS and observed in an inverted confocal microscope (Zeiss, LSM 980 with Airyscan 2/two-Photon Laser) using the FITC and DAPI channels and a 20X objective.

2.17. Statistical analysis

Analysis of variance was performed as statistical analysis with SPSS 29 (IBM, USA). Differences with a *p*-value < 0.05 were considered statistically significant.

3. Optical principles in laser-based DLP printing

3.1. Image formation mechanism and resolution

DLP printing relies on projecting an image of each cross-sectional layer of a 3D model onto a photosensitive resin, causing it to solidify. The image formation process in optical systems like DLP is fundamentally determined by the nature of light and its interaction with the optical components. Here, two primary types of illumination can be considered: coherent (such as lasers) and incoherent light (such as LEDs), each impacting the optical performance in distinct ways. Exploring these illumination types reveals critical differences in their optical behaviors, influencing the resolution and overall quality of printed objects.

For incoherent light, the image formation is described by the convolution of the object's intensity distribution with the system's point spread function (PSF) [25]:

$$I_{\text{image}}(x,y) = I_{\text{object}}(x,y) \otimes \text{PSF}(x,y). \quad (4)$$

In contrast, image formation involves the convolution of the object's amplitude distribution with the system's coherent spread function (CSF) for coherent light. The resultant complex amplitude image is then squared to obtain the intensity distribution [26]:

$$E_{\text{image}}(x,y) = E_{\text{object}}(x,y) \otimes \text{CSF}(x,y) \quad (5)$$

$$I_{\text{image}}(x,y) = \left| E_{\text{image}}(x,y) \right|^2. \quad (6)$$

In other words, in the case of incoherent light, the intensity is derived from the superposition of individual waves with randomly varying phase relationships. On the other hand, with coherent light, the waves maintain a constant phase relationship, leading to interference patterns that produce a complex amplitude, the square of which determines the intensity. Due to its different mechanisms of image formation, the optical transfer function (OTF) which defines how spatial frequencies of an object are transmitted through the system, varies significantly between coherent and incoherent light sources.

The OTF is directly related to the system's ability to reproduce the details of an object in an image, influencing the overall resolution and image quality [27]. For the coherent light sources, it is influenced by the phase coherence of the light waves and is represented as:

$$\text{OTF}_{\text{coherent}}(u,v) = \iint P(x,y) P(x-u,y-v)\,\mathrm{d}x\mathrm{d}y \quad (7)$$

where $P(x,y)$ represents the pupil function of the optical system and (u,v) are the spatial frequency coordinates. In contrast, for incoherent light sources, the OTF is primarily determined by the intensity distribution of the light and lacks phase information. The absence of phase coherence in incoherent light results in a different form of the OTF, which is expressed as the autocorrelation of the amplitude transfer function:

$$\text{OTF}_{\text{incoherent}}(u,v)$$
$$= \iint |P(x,y)|^2 |P(x-u,y-v)|^2 \mathrm{d}x\mathrm{d}y. \quad (8)$$

The absence of phase coherence in incoherent light sources generally results in smoother and more uniform image formation, thereby reducing interference artifacts. However, this characteristic typically leads to a lower resolution compared to coherent systems. On the other hand, coherent light systems can achieve higher contrast at high spatial frequencies due to constructive interference effects, enhancing the sharpness and detail of the image [28].

3.2. Diffraction characteristics of coherent and incoherent light

In DLP systems, where a DMD serves as the imaging element, it effectively acts as a diffraction grating due to the array of micromirrors that can selectively reflect or block light [29]. This grating-like behavior influences how light interacts and contributes to the final image. To further comprehend how image formation differs in DLP systems using coherent and incoherent light, it is essential to explore their diffraction characteristics.

In coherent systems, light diffracts in a manner where only two diffraction orders split some energy away from the zero order. The angle of diffraction is given by $\sin(\alpha) = \lambda/\omega$, where λ is the wavelength of the light and ω is the line width of the grating [30]. As these two side diffraction orders pass through the optical system's pupil, they interfere constructively with each other and the zero-order beams at the image plane. This interference forms a sinusoidal intensity distribution, which is modified only by the system magnification. As the grating frequency increases, the diffraction orders spread wider. In contrast, diffracted incoherent light fills the entire pupil. As the diffraction spread widens with increasing frequency, a portion of the light still passes through the pupil up to a frequency twice higher than that for coherent light. As the signal passing through becomes increasingly incomplete, its contrast transfer steadily declines toward the high-frequency cutoff since less and less information from the object reaches the image. Since incoherent sources exhibit a broader spread of spatial frequencies due to their lack of coherence-related interference patterns, filtering coherent sources to enhance image sharpness

is relatively straightforward. The peculiar diffraction behavior in coherent light systems allows for easier manipulation and filtering to achieve higher image quality.

3.3. Intensity-etendue trade-off

In the context of DLP printing, the etendue of light sources plays a pivotal role in determining system performance. Etendue is a conserved quantity in optical systems, representing the fundamental limit on how much light can be efficiently collected and manipulated in an optical system [31] as described by its mathematical formulation:

$$G = \iint (\cos\theta) \, \mathrm{d}A\mathrm{d}\Omega \qquad (9)$$

where G is the etendue, θ represents the angle between the normal vector of the differential area $\mathrm{d}A$ and the direction towards the center of the differential solid angle $\mathrm{d}\Omega$. To efficiently capture light from a given source, the etendue of the projector optics must exceed that of the source; otherwise, light loss occurs [32]. For a coherent beam, the solid angle Ω is minimal, leading to a small etendue value, which allows for precise control and high-resolution patterning. Conversely, incoherent light sources such as LEDs exhibit higher etendue due to their broader emission spectrum and lack of spatial coherence.

In DLP systems, the etendue is constrained primarily by two factors: the angular range of the micromirrors and the active area of the DMD [33]. The micromirrors rotate by $\pm\theta_{\mathrm{dmd}}$, establishing a half-angle illumination cone of θ_{dmd}, which directly determines the system's f-number and solid angle [34]:

$$F/\# = \frac{1}{2n\sin\theta_{\mathrm{dmd}}} \qquad (10)$$

$$\Omega = 2\pi \left(1 - \cos\theta_{\mathrm{dmd}}\right). \qquad (11)$$

Therefore, considering the DMD module used in our system, with a 12° tilt angle [35], this equates to an effective f-number of 2.4 or a solid angle of 0.137 steradians. Coherent lights offer distinct advantages in this scenario due to their minimal divergence and strong spatial coherence, resulting in emission angles significantly smaller than the broader solid angles typical of LEDs, such as those emitting up to 2π steradians depending on the optical system that is mounted [32].

3.4. Speckle reduction

Speckle formation is common when using coherent light sources, such as lasers. When a laser illuminates an object, the roughness of the illuminated surfaces in the optical system causes the scattered light to have components with different delays. As these components propagate further, they interfere with each other, producing a granular intensity pattern known

as speckle leading to non-uniform illumination and potential defects in the printed object. Several methods can be employed to mitigate speckle by reducing the temporal or spatial coherence of the laser, such as using multi-polarization [36], multi-wavelength [37], multi-angle illumination [38] techniques, or incorporating an optical diffuser [39], a spatial light modulator [40] or a Hadamard diffuser [41].

To address the possible speckle issue, we proposed a dual-laser configuration in our system. This system employs two lasers operating at the same wavelength, combined using a polarization beam splitter. One of the lasers passes through a half-wave ($\lambda/2$) waveplate to align its polarization with the other, and variable ND filters are used for both lasers to control their intensities. This setup offers several advantages. By combining two lasers with aligned polarizations, we reduce the overall spatial coherence, which helps to diminish coherent speckle formation. Additionally, the lack of phase and frequency correlation between the two laser sources eliminates temporal coherence, effectively averaging out speckles over time. The $\lambda/2$ waveplate ensures that both laser beams contribute equally, minimizing intensity fluctuations that could lead to speckles. Most importantly, the dual-laser system generates multiple independent speckle patterns. It was shown that if M-independent speckle patterns are combined, the speckle contrast decreases by a factor of $1/\sqrt{M}$ [28, 32, 42]. By combining the outputs of two lasers, we effectively double the number of independent speckle patterns. According to the principle of speckle contrast reduction, this reduces the speckle contrast by a factor of $1/\sqrt{2}$. In addition to the advantages provided by the dual-laser configuration, the diffusion effect during polymerization further mitigates the impact of any remaining speckles [43]. Thus, the polymerization process itself acts as a natural speckle reduction mechanism, contributing to smoother surfaces and higher fidelity in the printed objects.

4. Results and discussion

4.1. The design approach and principle of operation

To evaluate the performance variations resulting from transitioning from an LED to a laser light source in a DLP printing system, we have constructed a system capable of operating with either light source while maintaining all other system components constant (see figure 1(b)). This approach ensures that any observed performance differences can be directly attributed to the change in illumination method, thereby providing a clear and controlled comparison of the two light sources under similar operational conditions.

As illustrated in figure 1(b), both configurations direct the light sources, either a dual-laser system emitting coherent light or an LED torch providing
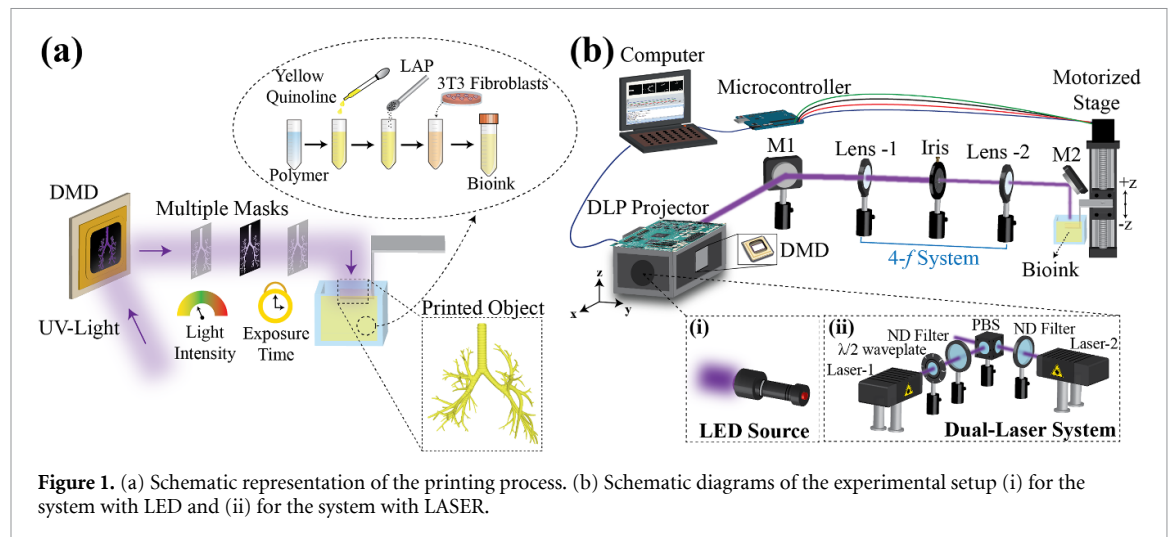
Figure 1. (a) Schematic representation of the printing process. (b) Schematic diagrams of the experimental setup (i) for the system with LED and (ii) for the system with LASER.

broad-spectrum illumination—into the DLP system. Within the DLP system, computer-controlled DMD mirrors precisely modulate these light sources. This modulation process generates the specific light patterns necessary for the layer-by-layer construction of the printed object. After modulation by the DMD, the light passes through a single aperture and is then directed to the 4f optical system. The single aperture in the system spatially filters and shapes the light beam, ensuring only the desired portion passes through, thereby enhancing the resolution and uniformity of the projected patterns. Then 4f system performs precise Fourier transforms of the light beam, enabling spatial filtering at the Fourier plane to enhance the clarity and resolution of the projected patterns. The filtered light is then directed onto a resin reservoir positioned on a linear stage. This stage moves along the z-axis, precisely adjusting each layer's position relative to the curing light. The synchronization of the linear stage movement with the modulation of the DMD is achieved through an Arduino controller, which controls the timing and sequence of operations. This synchronization ensures that each layer of the object being printed is accurately positioned relative to the modulated light pattern. By maintaining temporal alignment, the system maintains accurate layer-by-layer fabrication of objects with high precision and fidelity, critical for producing complex geometries and maintaining uniformity in the printed objects.

For the illumination component of our system, we have implemented two distinct configurations: one utilizing an LED torch providing incoherent illumination, as depicted in figure 1(b), and the other employing a dual-laser system emitting coherent light, both operating in the UV spectrum. To establish the dual-laser system, two coherent UV lasers at 405 nm were polarization multiplexed to create a single, coherent light source, as illustrated in figure 1(b). Here, each beam is precisely aligned to ensure optimal beam overlapping and uniform

intensity distribution after the polarization beam splitter, which allows us to merge their paths. To achieve uniform polarization, a $\lambda/2$ plate is employed to adjust the polarization state of one laser beam, ensuring it matches the axis of the polarization beam splitter. Additionally, variable ND filters were utilized for both lasers to precisely control the intensity of each laser beam independently, allowing for precise control over the combined beam's overall power. This combined, coherent light was then directed into the DMD for pattern modulation. The combined output of two lasers not only reduces speckle but also improves the overall light distribution, providing a more reliable and consistent curing process.

4.2. Analysis of printing resolution and intensity impact

In DLP bioprinting, achieving high printing resolution is crucial for producing detailed and accurate three-dimensional objects. The resolution of DLP systems is influenced by various factors, including the type of light source and its intensity. This section explores the detailed analysis of printing resolution in both UV-LED and dual-laser DLP systems while examining how the intensity of the light source affects the overall printing quality. By focusing on laser sources alone, we investigate how varying intensities impact the quality and precision of printed objects. Through this analysis, we aim to elucidate their impact on the quality and precision of printed objects, providing insights into optimizing DLP processes for diverse manufacturing applications.

To evaluate the resolution capabilities of the systems, we conducted a systematic procedure involving printing test strips with varying widths. Figure 2(a) presents a schematic representation of masks featuring varying strip widths, which serve as test patterns to assess the system's ability to reproduce fine details. Each mask configuration is precisely designed to test specific width parameters critical for resolution evaluation. For each width category, we systematically
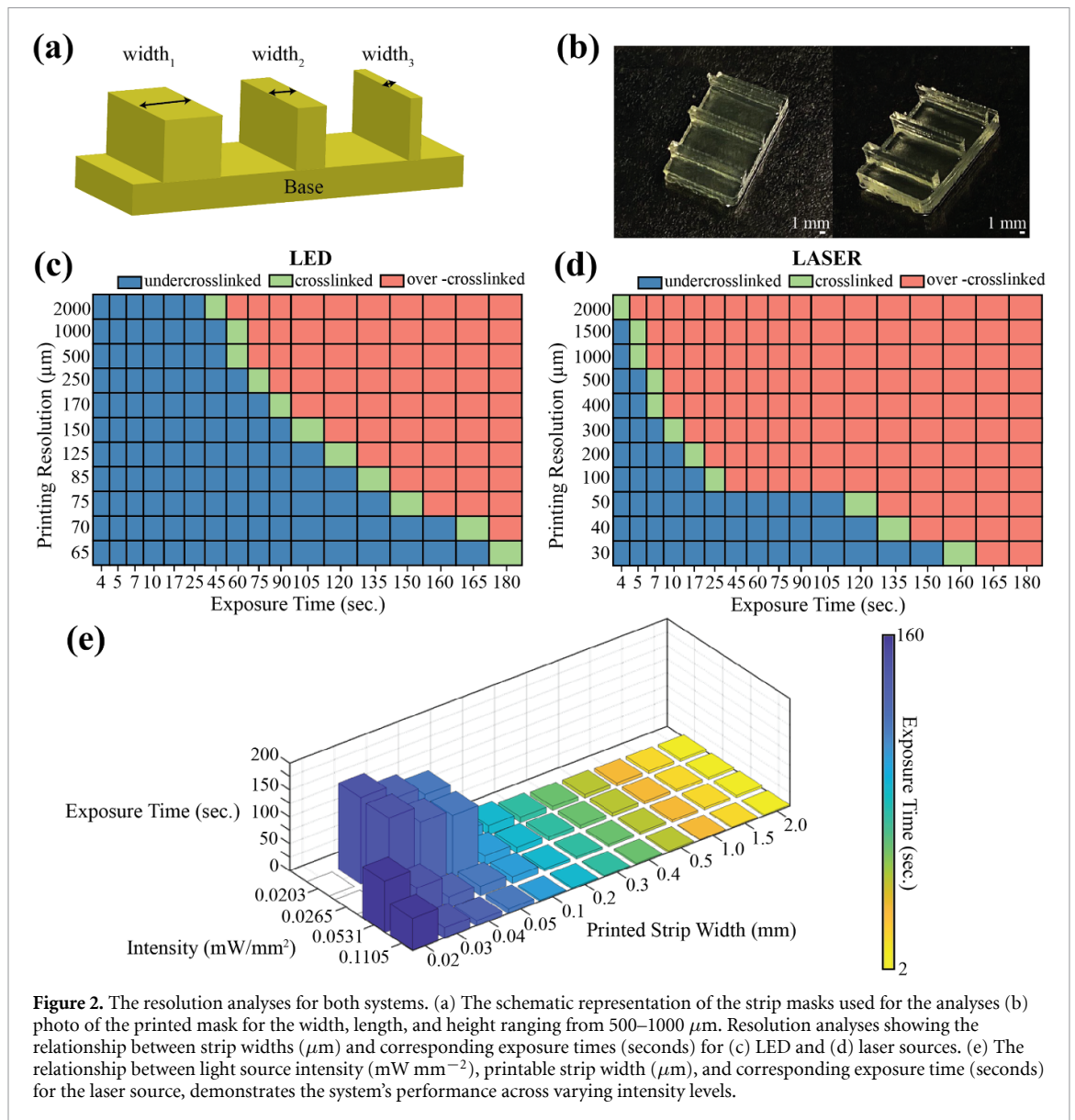
Figure 2. The resolution analyses for both systems. (a) The schematic representation of the strip masks used for the analyses (b) photo of the printed mask for the width, length, and height ranging from 500–1000 μm. Resolution analyses showing the relationship between strip widths (μm) and corresponding exposure times (seconds) for (c) LED and (d) laser sources. (e) The relationship between light source intensity (mW mm^{-2}), printable strip width (μm), and corresponding exposure time (seconds) for the laser source, demonstrates the system's performance across varying intensity levels.

varied the exposure time of the sources. Figure 2(b) displays photographs of the printed masks, showcasing the actual results obtained from the DLP printing process. This variation allowed us to determine the minimum exposure time required to accurately and consistently cure the resin for each strip width, thereby establishing a direct correlation between exposure time and achievable resolution.

In figures 2(c) and (d), we present the relationship between printed width and the corresponding required exposure time for both LED and laser sources, each operating at the same light intensity of 0.0203 mW mm^{-2}. The findings reveal distinct differences in the achievable resolution and efficiency between the two light sources. For the LED source, the minimum achievable printed width is observed to be 65 μm, while the laser source achieves a finer resolution with a minimum width of 30 μm. Moreover, the data highlights a substantial reduction in the required exposure time when using the laser source compared

to LED. For instance, printing a width of 1000 μm requires approximately 60 s with the LED source, whereas the laser achieves the same width in just 5 s. This finding underscores the superior efficiency and precision of the laser source in DLP printing applications, enabling faster fabrication times and finer feature resolution.

As a next step, further exploration is conducted to assess the effects of varying light intensity on DLP printing performance presented in figure 2(e). We systematically varied the system's light intensity by incrementally adjusting adjustable neutral ND filters. As expected, increasing the light intensity corresponded to the capability to print smaller features, demonstrating a direct relationship between intensity and achievable resolution. For instance, increasing the light intensity from 0.0203 to 0.0531 mW mm^{-2} enabled the printing of finer features, reducing the minimum achievable strip width to 20 μm. Concurrently, the required exposure time for printing
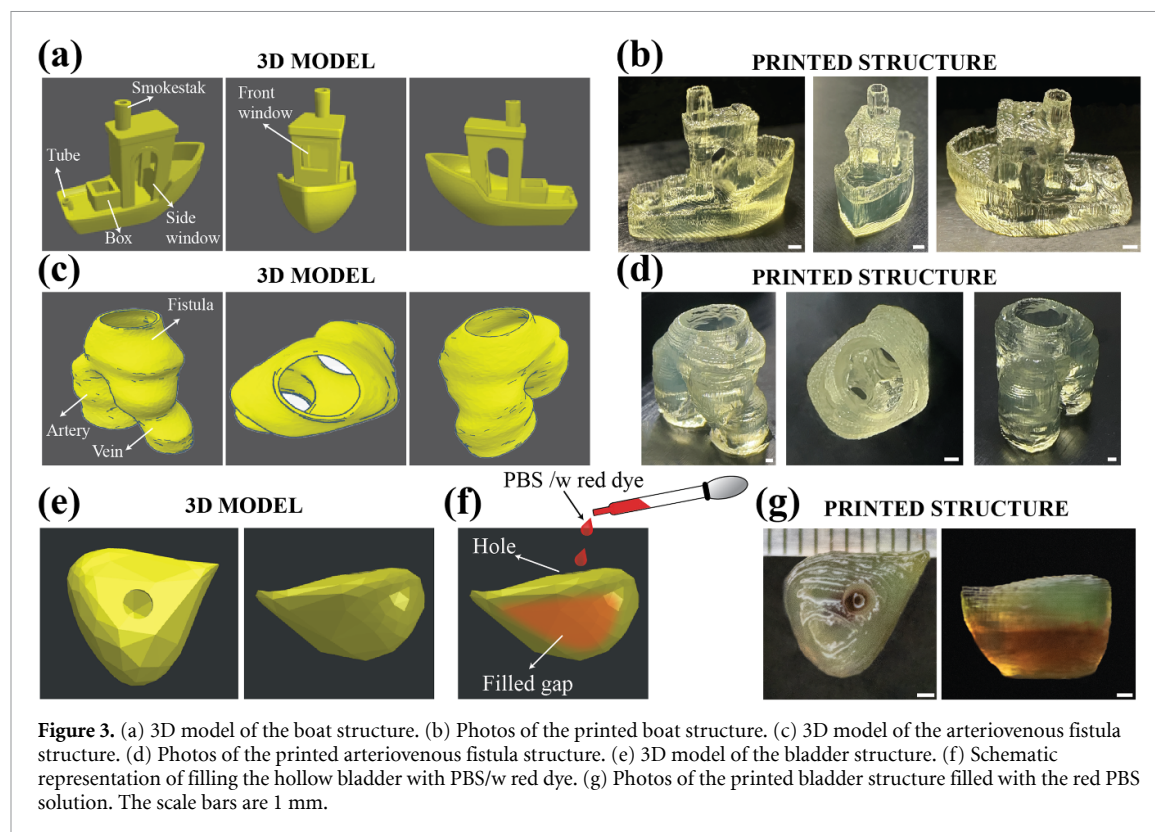
Figure 3. (a) 3D model of the boat structure. (b) Photos of the printed boat structure. (c) 3D model of the arteriovenous fistula structure. (d) Photos of the printed arteriovenous fistula structure. (e) 3D model of the bladder structure. (f) Schematic representation of filling the hollow bladder with PBS/w red dye. (g) Photos of the printed bladder structure filled with the red PBS solution. The scale bars are 1 mm.

also decreased significantly. Notably, while it took 10 s to print a 300 μm-wide strip at 0.0203 mW mm^{-2}, this exposure time was reduced to 7 s, 4 s, and finally, 3 s as the intensity increased to 0.0265 mW mm^{-2}, 0.0531 mW mm^{-2}, and 0.1105 mW mm^{-2}, respectively. This finding underscores the direct relationship between light intensity, feature resolution, and printing efficiency in laser-based DLP systems. Higher intensities not only enable the fabrication of finer details but also expedite the overall printing process, demonstrating the system's capability to achieve enhanced precision and productivity with optimal light intensity management.

4.3. Evaluation of complex structure printing with laser-based DLP system

To demonstrate the capability of our laser-based DLP system in printing complex structures, we fabricated three distinct models: a boat structure, an arteriovenous fistula structure, and a bladder structure. These models were chosen to represent a range of geometric complexities and relevance to biomedical applications. The procedure for printing these models involved several critical steps to ensure accuracy and fidelity. First, the 3D models of the boat, arteriovenous fistula, and bladder structures were designed. These digital models were then processed and sliced into layers suitable for the DLP printing process. Each layer was meticulously patterned using computer-controlled DMD mirrors to ensure precise replication of the design. For these characterizations, PEGDA ink was used. We used an intensity of

0.1105 mW mm^{-2}, which provides the highest resolution and fastest crosslinking time. Depending on the features of each model, the required exposure times and the thickness of each layer were optimized to ensure the best possible print quality. As illustrated in figure 3, the first part shows the 3D CAD models of these structures, followed by photographs of the corresponding printed objects.

The boat structure serves as a benchmark for assessing the system's ability to produce detailed and fine features, such as the hull and deck components (see figures 3(a) and (b)). The total printing time for the boat structure was 12 min, with the maximum exposure time for one layer being 20 s and the minimum time being 10 s. As seen in figure 3(b), the successful fabrication of the boat structure underscores the laser-based DLP system's high resolution and accuracy, demonstrating its potential for producing detailed and precise models. Also, the accompanying table 1 provides a quantitative assessment, presenting the design dimensions versus the measured dimensions of the printed objects. Three samples were measured for each pattern to evaluate the system's printing precision. There was a negligible deviation (0.05%–1.16%) between the measured and designed structural parameters, indicating precise alignment and placement, which is attributed to tiny over-curing. However, the slight differences between the measured and designed widths revealed that the proposed projection-based printing technique has relatively acceptable accuracy and resolution.

Table 1. The dimension of the original boat, arteriovenous fistula, and bladder designs after projection and printed patterns ($n = 6$).

	Parameters		Design dimensions (mm)	Measured dimensions (mm)	Percentage error (%)
Boat	Width	W	7.613	7.601 ± 0.0066	0.15
	Length	L	14.697	14.868 ± 0.0253	1.16
	Smokestak	h_{st}	2.000	2.021 ± 0.0035	1.05
		D_{st}	1.910	1.910 ± 0.0055	n.a.
	Side-window	h_{sw}	5.150	5.146 ± 0.0036	0.08
		W_{sw}	2.166	2.165 ± 0.0081	0.05
	Front-window	h_{fw}	2.350	2.358 ± 0.0102	0.34
		w_{fw}	2.532	2.533 ± 0.0201	0.04
	Behind box	w_{bb}	2.645	2.631 ± 0.0232	0.53
		L_{bb}	1.751	1.749 ± 0.0063	0.11
	Behind tube	D_{bt}	1.433	1.436 ± 0.0278	0.21
Arteriovenous fistula	Width	W	14.928	14.921 ± 0.0106	0.05
	Height	H	14.475	14.484 ± 0.04	0.06
	Fistula	D_f	5.789	5.788 ± 0.0560	0.02
		t_f	0.1745	0.1749 ± 0.0004	0.23
	Vein	D_v	5.956	5.954 ± 0.0963	0.03
		t_v	1.3154	1.3157 ± 0.0024	0.02
	Artery	D_a	6.584	6.583 ± 0.0473	0.02
		t_a	1.1336	1.1338 ± 0.0036	0.02
Bladder	Width	W	7.903	7.902 ± 0.0397	0.02
	Length	L	10.261	10.251 ± 0.0164	0.10
	Height	H	9.650	9.668 ± 0.0325	0.19
	Hole diameter	D	2.071	2.076 ± 0.0480	0.24

As depicted in figures 3(c) and (d), the arteriovenous fistula model, consisting of two hollow tubes (vein and artery) that merge at a certain point (fistula), was selected to showcase the system's capability to accurately replicate complex tubular structures. This design illustrates the system's precision in fabricating geometries where multiple components join seamlessly, demonstrating its potential for applications requiring intricate and interconnected structures. The total printing time for the arteriovenous fistula structure was 12.5 min, with the maximum exposure time for one layer being 18 s and the minimum time being 4 s. A detailed comparison between the designed and printed dimensions, including the width and height of the entire structure, as well as the diameter and wall thickness of the fistula, vein, and artery components, was conducted. The results indicate a maximum percentage error of 0.23% and a minimum of 0.02%, underscoring the system's high precision in fabricating complex models.

Lastly, the bladder structure exemplified the system's versatility in printing organ-like structures, highlighting its potential in biomedical research and regenerative medicine. The bladder model, printed as a hollow structure with a precisely placed hole at the top, was used to illustrate the system's ability to fabricate internal cavities and complex shapes. To validate the hollowness, we injected red PBS solution through the top hole, visually confirming the successful creation of the internal cavity. This capability is particularly important for applications requiring the production of functional biomedical devices and implants with internal channels or reservoirs. The bladder structure was printed in a total time of 7 min, with the exposure time per layer ranging from a maximum of 15 s to a minimum of 3 s. A comparison between the designed and printed dimensions, encompassing the width, length, and height of the entire model, as well as the diameter of the hole is provided in table 1. The results indicate a maximum percentage error of 0.24% and a minimum of 0.02%.

The data demonstrates a high degree of accuracy in the printed models, with minimal deviation from the intended design specifications. These analyses underline the versatility and precision of the laser-based DLP system in producing complex and functional structures. The ability to accurately fabricate such models is critical for advancing applications in medical device manufacturing, tissue engineering, and other high-precision fields, demonstrating the laser-based DLP system's potential to meet diverse and demanding fabrication requirements.

4.4. Segmented printing technique and system dynamic range analyses

Achieving precise control over crosslinking is critical in the DLP printing process to ensure high-quality output and minimize defects. Over-crosslinking, which results from excessive exposure to the light source, can compromise the integrity and resolution of printed structures. This phenomenon is influenced by several key factors including light scattering, depth of focus/penetration depth, and molecular diffusion [44, 45].
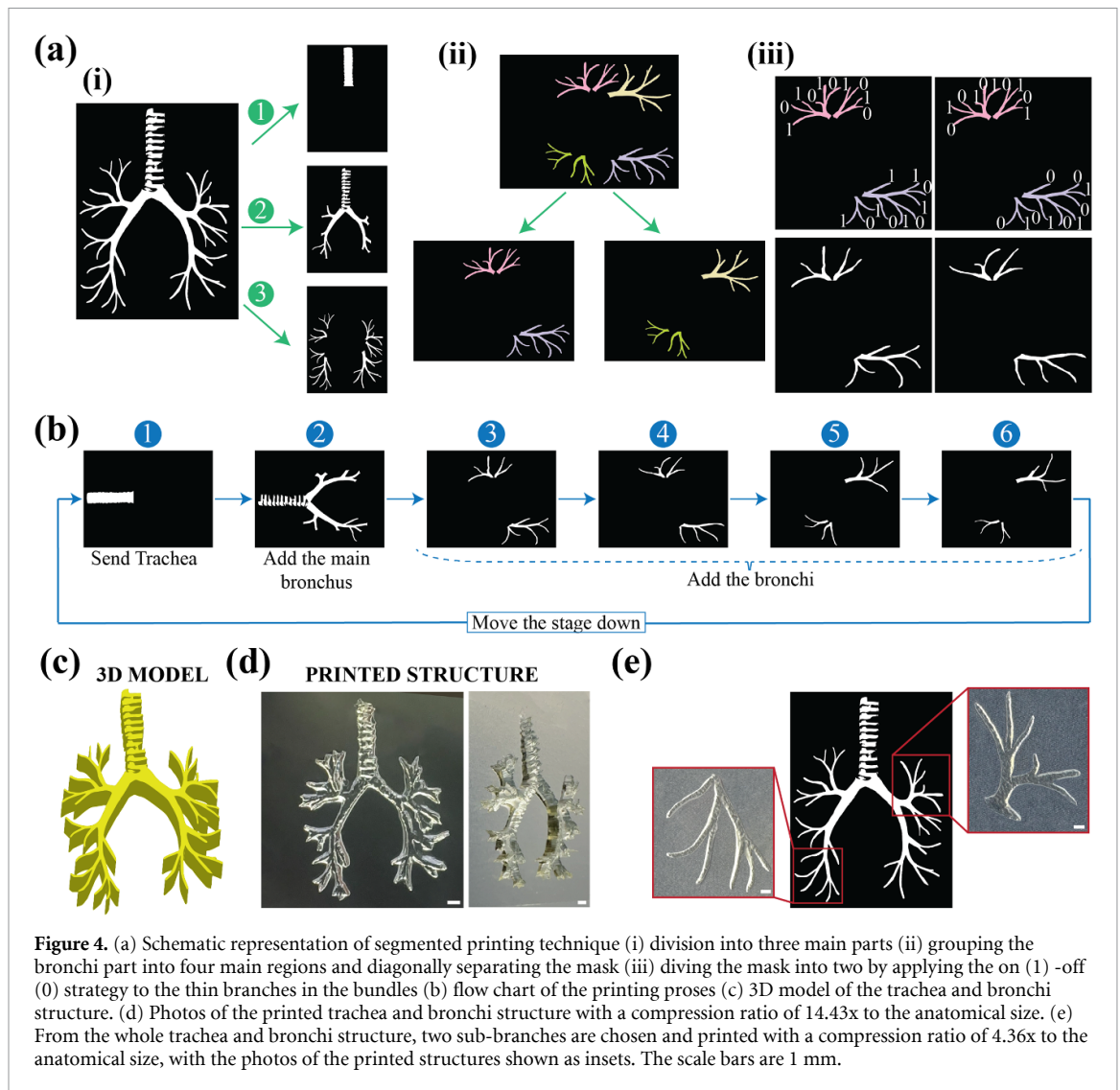
Initially, the hydrogel used in our system is a transparent liquid. Upon polymerization, however, it becomes translucent, which can cause scattering of the light. This scattering effect can induce non-uniform exposure, thereby potentially causing over-crosslinking in localized areas, which subsequently impacts the overall resolution of the printed structures [46]. Furthermore, light penetration and polymerization within the hydrogel are constrained to specific depths determined by the wavelength of the light source and the material composition. This limitation primarily affects the vertical resolution of printed structures but can also disrupt their lateral resolution. By incorporating light-absorbing agents into the medium, the depth of cure can be notably decreased, effectively regulating the extent of polymerization [47]. This adjustment is critical for mitigating excessive crosslinking in deeper layers, which might otherwise introduce inconsistencies in the structural integrity of the printed objects. Lastly, free-radical photopolymerization comprises several sequential stages: initiation, propagation, chain transfer, and termination [48]. While free radicals are initially generated solely within the region illuminated by light, these radicals, along with propagating polymer chains, have the potential to diffuse beyond the intended areas of illumination. This diffusion phenomenon results in undesired polymerization extending beyond the targeted regions, thereby contributing to over-crosslinking.

To overcome the adverse effects of over-crosslinking, several innovative solutions have been proposed in the literature. One approach involves synthesizing a new photoinhibiting additive, curcumin–Na (Cur–Na), which has been shown to reduce light penetration and mitigate scattering [49]. By limiting the depth of light penetration, Cur–Na effectively controls the polymerization process, thereby enhancing the precision of printed structures. Another method substitutes the trapped resin with a UV-blocking liquid to mitigate print-through or unwanted polymerization [50]. This technique not only improves vertical resolution but also maintains the clarity of fine details in the printed object. Furthermore, light exposure delivered in millisecond-scale 'flashes' instead of continuous light exposure has proven effective in controlling polymerization [51]. Flashing exposure generates a large number of free radicals that continue polymerizing and opacifying the material in the dark. This method, with exposure times of 10 ms and flashing intensities as high as 120 W cm^{-2}, allows for precise control over the polymerization process, reducing the likelihood of over-crosslinking and enhancing the overall resolution of the printed structures. The first two methods emphasize material optimization to achieve controlled and uniform polymerization: synthesizing a novel photo-inhibiting additive to reduce light penetration and scattering and substituting trapped resin with a UV-blocking liquid to prevent print-through and enhance vertical resolution. In contrast, the final approach leverages the inherent properties of the free radical photopolymerization process itself.
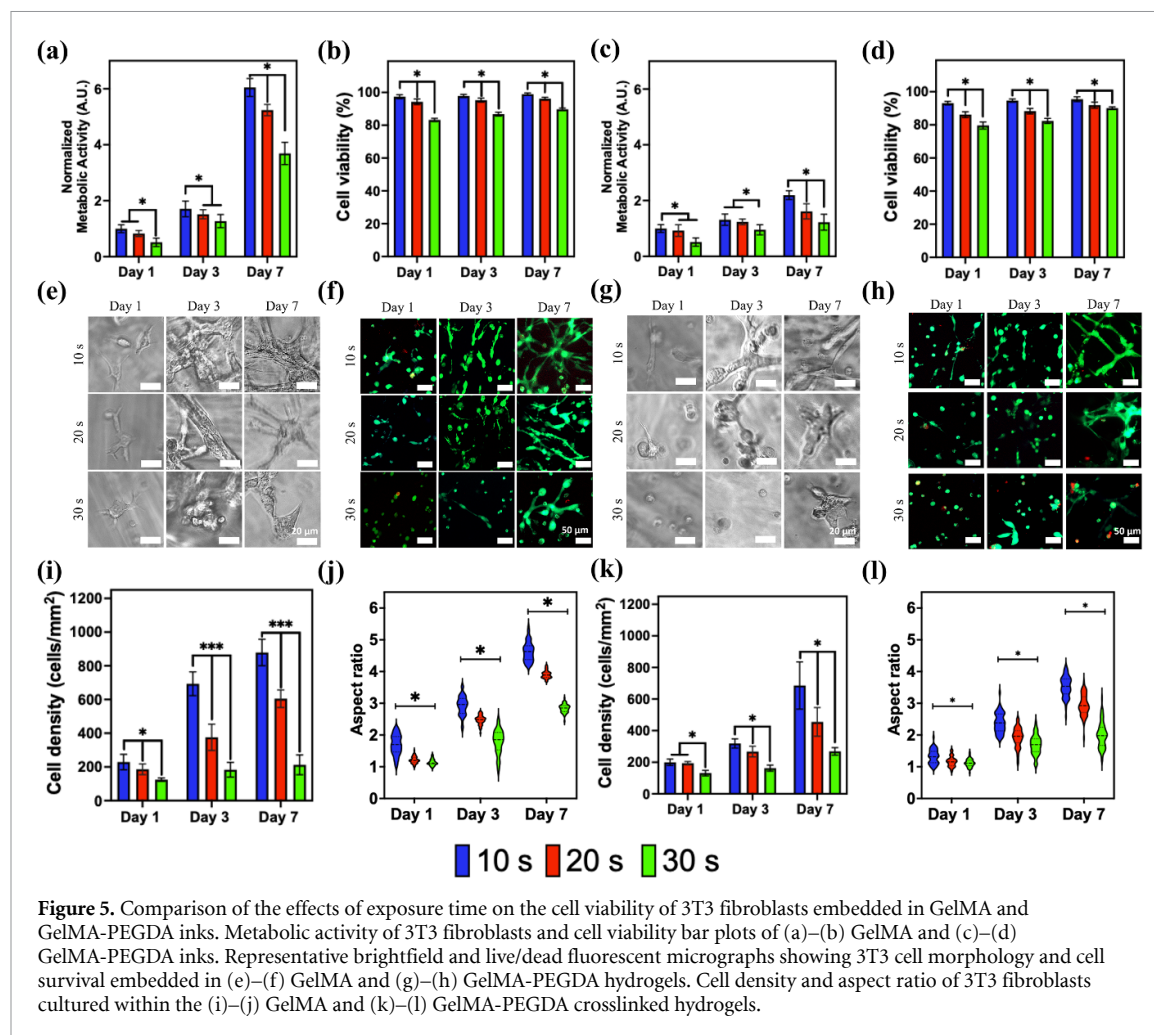
To address over-crosslinking due to molecular diffusion, we implemented a segmented printing technique that also leverages the multi-stage characteristics of free radical photopolymerization. For this characterization, we used PEGDA ink to ensure controlled polymerization and minimize over-crosslinking effects. As a demonstration, we focused on a trachea-bronchi model featuring intricate bronchial structures with narrow gaps. Initially, we segmented the photomask into three main parts to control the diffusion of the activated photoinitiator. This segmentation strategy was based on varying thicknesses across the model: thicker sections generate higher total intensity and more free radicals, which can diffuse and accumulate in thinner areas, leading to over-crosslinking.

To mitigate this effect, we segmented and printed these parts separately while superimposing the masks to minimize diffusion between adjacent regions. We further refined this segmentation by grouping the bronchial branches into four clusters, positioning diagonal parts together to increase distances between potential crosslinking sites, and reducing diffusion pathways. Additionally, we employed an on (1)- off (0) segmentation strategy within each bundle of bronchial branches, alternating the activation of adjacent branches to create spatial gaps and block diffusion effects more effectively. This multi-layered segmentation approach aimed to optimize polymerization conditions by spatially separating illuminated regions and minimizing the impact of diffusion on structural fidelity and resolution in our printed trachea-bronchi model. The segmentation process is outlined in figure 4(a), illustrating the division of the mask into distinct sections to mitigate over-crosslinking effects due to molecular diffusion. Additionally, the printing workflow is detailed in the flowchart provided in figure 4(b). Following the segmentation approach to mitigate over-crosslinking in the segmental bronchus model, we successfully enhanced the printing quality but as can be seen in figure 4(d) complete elimination of over-crosslinking in narrow gaps remained challenging. Subsequently,

Figure 4. (a) Schematic representation of segmented printing technique (i) division into three main parts (ii) grouping the bronchi part into four main regions and diagonally separating the mask (iii) diving the mask into two by applying the on (1) -off (0) strategy to the thin branches in the bundles (b) flow chart of the printing proses (c) 3D model of the trachea and bronchi structure. (d) Photos of the printed trachea and bronchi structure with a compression ratio of 14.43x to the anatomical size. (e) From the whole trachea and bronchi structure, two sub-branches are chosen and printed with a compression ratio of 4.36x to the anatomical size, with the photos of the printed structures shown as insets. The scale bars are 1 mm.

we have conducted dynamic range analyses aimed at optimizing the system's compression ratio to potentially reduce crosslinking effects. In this context, dynamic range refers to the system's ability to accurately reproduce both fine details and larger features across a broad range of contrast levels at a specified magnification. This analytical approach explores the impact of altering the system's optical compression settings, hypothesizing that increasing the gap dimensions could mitigate over-crosslinking by enhancing spatial separation between printed features, which also shows the system printing limit regarding the magnification. Due to limitations in the system's optical configuration, comprehensive magnification of the entire structure was impractical without modifications to lenses and mirrors. Instead, we adopted a targeted approach where the target areas were systematically selected for analysis and incrementally adjusted their structural parameters to identify an optimal compression ratio that minimizes over-crosslinking while preserving structural integrity. Here, compression ratio refers to the proportional scaling factor applied to the dimensions of the printed structure

relative to its real anatomical size. By referencing real anatomical dimensions, particularly focusing on adult female tracheal measurements from established literature [52], we assessed the fidelity of our printing process. Comparing the printed structure size depicted in figure 4(c) with these anatomical values revealed that our system's compression ratio was approximately 14.43x. Subsequently, to optimize printing outcomes and mitigate issues such as over-crosslinking that could potentially obstruct bronchial pathways, we targeted specific regions, as highlighted in figure 4(e) inset. Through systematic adjustment of the compression ratio, we observed that reducing it to 4.36x enabled the successful printing of these structures without encountering over-crosslinking issues that could potentially obstruct the gaps between the bronchi. These findings show the critical role of dynamic range management in DLP printing for achieving high-quality, precise models. While our system demonstrates proficiency in printing intricate structures, optimizing dynamic range is essential for further enhancing printing outcomes. This process can be effectively executed by adjusting the

Figure 5. Comparison of the effects of exposure time on the cell viability of 3T3 fibroblasts embedded in GelMA and GelMA-PEGDA inks. Metabolic activity of 3T3 fibroblasts and cell viability bar plots of (a)–(b) GelMA and (c)–(d) GelMA-PEGDA inks. Representative brightfield and live/dead fluorescent micrographs showing 3T3 cell morphology and cell survival embedded in (e)–(f) GelMA and (g)–(h) GelMA-PEGDA hydrogels. Cell density and aspect ratio of 3T3 fibroblasts cultured within the (i)–(j) GelMA and (k)–(l) GelMA-PEGDA crosslinked hydrogels.

focal length within the 4*f* system and modifying the dimensions of lenses and mirrors.

4.5. Effect of the use of the exposure time in the cell viability

The photopolymerization of hydrogels is a crucial step in the biofabrication process, where the exposure time and the intensity of the light source are the primary factors affecting cell viability [53]. The exposure of cells to UV light may damage them either by the direct interaction of the photons with the cellular DNA or by generating the reactive oxygen species (ROS), where these free radicals affect cell membranes [22, 54, 55]. Since they correlated with exposure time, we performed analyses to investigate the impact of exposure duration in 3T3 fibroblasts embedded in GelMA and GelMA-PEGDA bioinks. The bioinks were photopolymerized by varying the exposure time (10, 20, and 30 s). The effects of exposure time on cell viability and proliferation were evaluated by measuring metabolic activity, cell viability, observing the cell morphology, calculating the aspect ratio of cells, and measuring cell density over time, as shown in figure 5. To better illustrate the effect of exposure time on metabolic activity, and based on the assumption that samples exposed to lower light

intensities will experience less damage, we normalized the metabolic activity of the samples using the measurement of the samples crosslinked for 10 s on day 1 for each ink. As shown in figures 5(a) and (c), normalized metabolic activity showed a more than 40% reduction between samples crosslinked for 10 and 30 s on day 1, indicating a decrease in cellular metabolic function with increased crosslinking time. This trend was observable on day 3 and confirmed on day 7 when for the two inks, samples exposed to light for different times showed statistically different metabolic activities ($p < 0.05$). However, all three conditions still support cell growth, albeit starting from different baseline levels. Notably, GelMA bioinks exhibited up to a sixfold increase in metabolic rate across the different crosslinking times, whereas GelMA-PEGDA samples showed a twofold increase.

To corroborate the effect of crosslinking time on cell wellness, we evaluated the viability of 3T3 fibroblasts embedded in the hydrogels using a Live/Dead assay and calculated cell viability within the same time windows as the metabolic activity measurements. On day 1, for GelMA ink, cell viability was measured at $97.36 \pm 1.23\%$, $94.25 \pm 1.68\%$, and $83.21 \pm 0.98\%$ for samples crosslinked for 10, 20, and 30 s, respectively (figure 5(b)). For GelMA-PEGDA

bioinks, initial cell survival was $93.11 \pm 1.06\%$, $86.17 \pm 1.72\%$, and $79.62 \pm 2.18\%$ for samples crosslinked for 10, 20, and 30 s, respectively (figure 5(d)). Notably, GelMA hydrogels exposed to 30 s of crosslinking showed a statistically significant difference in viability compared to samples crosslinked for 20 and 10 s ($p < 0.05$). These differences are maintained during the 7 d of the experiment, where all samples are statistically different ($p < 0.05$) from each other, likely due to the inability of the surviving cells to proliferate. Representative micrographs from the experiment are shown in figures 5(f) and (h). The cell viability analysis demonstrated a correlation between exposure time and cell survival throughout the experimental period, with higher crosslinking times negatively affecting cell viability for both materials.
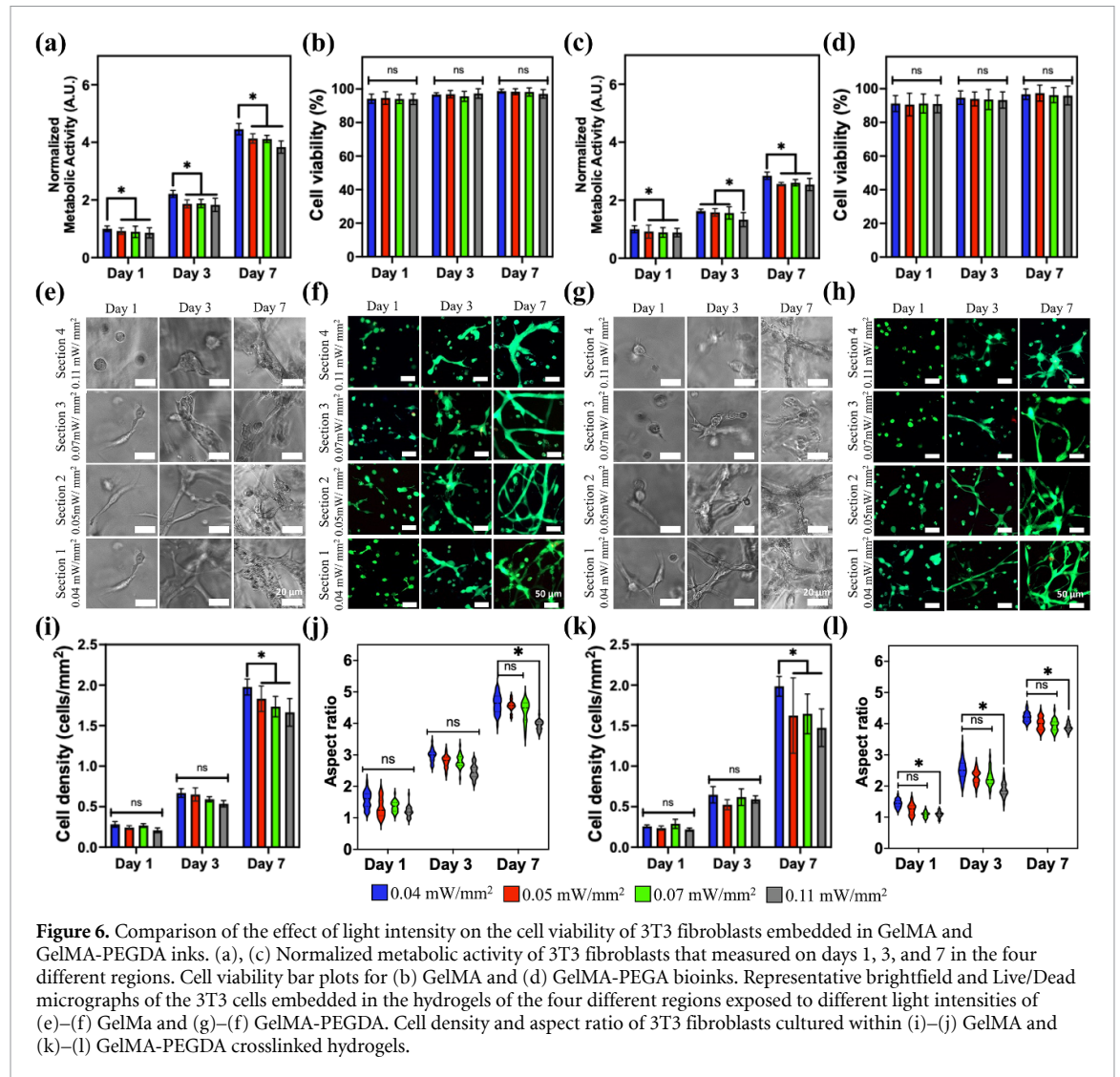
During the culture period, the morphology of the embedded 3T3 cells was studied using phase-contrast microscopy (figures 5(e) and (g)) and quantitatively assessed from fluorescent micrographs through aspect ratio measurements, as shown in the graphs in figures 5(j) and (l). After 1 d of culture, cells embedded in GelMA appeared more spread out and exhibited a more elongated morphology than fibroblasts embedded in GelMA-PEGDA, where cells appeared more rounded. However, the same effect was observed when the samples were exposed to longer crosslinking times. On day 3, GelMA samples crosslinked for 10 and 20 s exhibited the formation of fibroblast networks, whereas, in GelMA-PEGDA, this was only observable in the sample crosslinked for 10 s. The quantitative measurements of the aspect ratio of the cells (longest length/shortest length) show that, for both bioinks and all conditions on day 1, the aspect ratio was close to 1. However, samples crosslinked for 10 s displayed an extended distribution in the violin plot, attributed to the initial elongation of fibroblasts, while some cells still retained a rounded shape. This phenomenon was reversed after 7 d of culture, where samples crosslinked for shorter periods exhibited a narrower distribution compared to those crosslinked for extended periods. This change is attributed to the increased difficulty cells experience in elongating, with cells in longer crosslinked samples retaining a more rounded shape. By the final day of the experiment, GelMA bioinks achieved an aspect ratio ranging between 5 and 3, while GelMA-PEGDA bioinks showed a distribution between 3.5 and 2. Nonetheless, the fibroblasts' elongation was observed in all GelMA samples, while the cells in GelMA-PEGDA appeared more rounded and clustered. The observed morphological differences can be attributed to variations in hydrogel stiffness, which are associated with crosslinking density and influenced by differing exposure times. Increased stiffness is known to influence key aspects of cell behavior, such as adhesion, spreading, and cytoskeletal organization, which helps explain these observed changes [56, 57]. Additionally, mechanotransduction plays a

crucial role in activating metabolic pathways [58], affecting processes like glucose consumption [59], mitochondrial activity [60], and ATP production [61]. In the context of 3D bioprinting, optimizing hydrogel stiffness is essential for supporting cellular functions effectively. Fine-tuning hydrogel properties along with the printing protocol are necessary to identify the optimal balance that promotes both cellular elongation and proliferation.

The number of 3T3 cells was characterized over time to calculate cell density (total number of cells per mm^2) in GelMA and GelMA-PEGDA hydrogels, using image analysis (figures 5(i) and (k)) [62]. The cell density of 3T3 cells embedded in GelMA on day 1 was 242.79 ± 31.69, 185.87 ± 31.64, and 124.82 ± 9.40 cells mm^{-2} for exposure times of 10, 20, and 30 s, respectively. All samples are statistically different over time ($p < 0.05$). Conversely, the 3T3 cell density in GelMA-PEGDA on day 1 was 199.59 ± 19.98, 194.10 ± 10.73, and 130.31 ± 17.40 cells mm^{-2} for exposure times of 10, 20, and 30 s, respectively. In this material, the samples exposed for 30 s are statistically different from those exposed for shorter times. On the last day of the experiment, there is a significant difference in cell density as a function of exposure time for both GelMA and GelMA-PEGDA. The over-crosslinking caused by longer exposure times likely induced early apoptosis, restricting cell spreading and promoting detachment from the bioprinted constructs [63]. It is important to note that cellular debris and apoptotic bodies were excluded from the cell counts; thus, the observed reduction in cell density on day 1 is primarily attributed to cell death resulting from light exposure. The differences in metabolic activity and cell density across samples correlate with exposure time, indicating that longer light exposure negatively impacts cell viability and overall health, resulting in reduced cell viability.

4.6. Effect of the light intensity on cell viability

The threshold intensity in 3D bioprinting is the minimum power per unit area of light required to initiate the crosslink of a bioink. Higher laser intensities enhance the photopolymerization rate, leading to more solid structures and improved printing resolution until a certain point. Beyond this point, excessive light intensities may result in over-crosslinking. Overexposing bioinks to high light intensities may damage the cells, impacting long-term cell viability. To test the effect of light intensity on cellular responses in bioprinted constructs, we use the DMD chip to create graded intensity distributions. By keeping the exposure time constant, we printed a single structure with four distinct regions having graded intensity distributions of 0.044, 0.057, 0.077, and 0.11 mW mm^{-2}, labeled as regions 1, 2, 3, and 4, respectively. After printing, the sections were separated and cultured individually for cell viability

Figure 6. Comparison of the effect of light intensity on the cell viability of 3T3 fibroblasts embedded in GelMA and GelMA-PEGDA inks. (a), (c) Normalized metabolic activity of 3T3 fibroblasts that measured on days 1, 3, and 7 in the four different regions. Cell viability bar plots for (b) GelMA and (d) GelMA-PEGA bioinks. Representative brightfield and Live/Dead micrographs of the 3T3 cells embedded in the hydrogels of the four different regions exposed to different light intensities of (e)–(f) GelMa and (g)–(f) GelMA-PEGDA. Cell density and aspect ratio of 3T3 fibroblasts cultured within (i)–(j) GelMA and (k)–(l) GelMA-PEGDA crosslinked hydrogels.
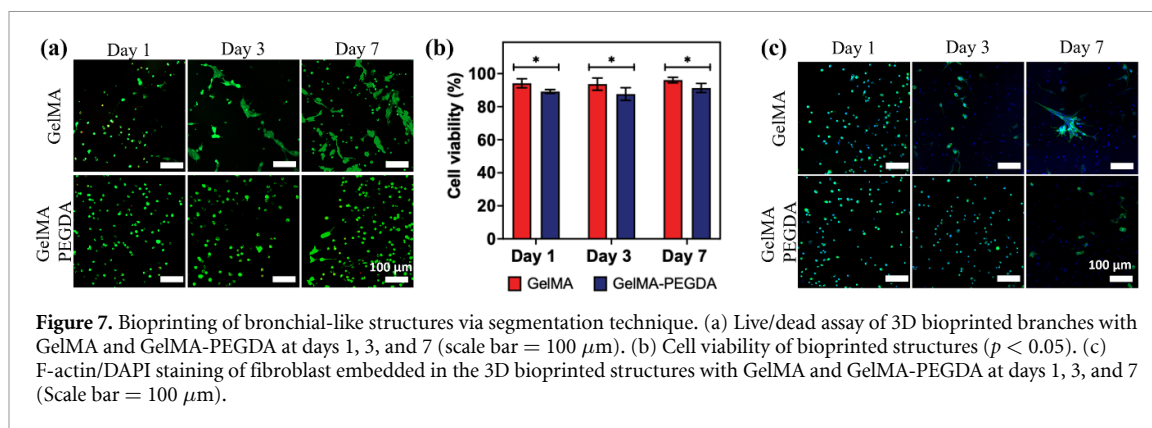
experiments (figures 6 and S1). Similar to the previous section, the effect of light intensity on 3T3 cells embedded in GelMA and GelMA-PEGDA is presented in figures 6(a) and (c). The metabolic activity of each region was normalized to the metabolic activity measured in the sample exposed to 0.04 mW mm^{-2}, assuming that lower light intensity resulted in less damage.

The metabolic activity for the GelMA bioink, measurements on day 1 shows that region 1, exposed to the lowest light intensity, has slightly higher metabolic activity than the other three regions ($p < 0.005$). This trend is also observed on days 3 and 7, with the metabolic activity of regions 2, 3, and 4 not being statistically different from each other on any of the days measured. Similarly, in the GelMA-PEGDA bioink, the metabolic activity in region 1 remained distinct from that in regions 2, 3, and 4 on days 1, 3, and 7. In both bioinks, metabolic activity increased in all regions over time, suggesting cell proliferation. Notably, the growth ratio from day 1 to day 7 was consistent across all regions, exhibiting an approximately 1.5-fold increase in metabolic activity. When

analyzing cell viability (figures 6(b) and (d)), both materials exhibited stable cell viability, maintaining levels above 90% throughout the seven-day culture period. This indicates that while variations in light intensity may influence metabolic activity to some extent, they do not have a direct impact on cell survival.

The effect of light intensity on cell morphology was documented using phase contrast and fluorescent micrographs of 3T3 cells embedded in GelMA and GelMA-PEGDA, exposed to different light intensities. The micrographs of the GelMA bioinks show that cells in regions 1, 2, and 3 exhibit a more spread and elongated morphology than those in region 4, where the cells appear more rounded (figures 6(e)–(h)). Similarly, cells in the GelMA-PEGDA hydrogels displayed modest elongation across all four sections on day 1. Figures 6(j) and (l) presents the quantitative measurements of the aspect ratio on day 1, revealing that all treatments had cell populations with ratios between 1 and 2, indicating a mix of round cells and cells beginning to elongate. The distribution range of aspect ratios in the four regions decreased as light

Figure 7. Bioprinting of bronchial-like structures via segmentation technique. (a) Live/dead assay of 3D bioprinted branches with GelMA and GelMA-PEGDA at days 1, 3, and 7 (scale bar = 100 μm). (b) Cell viability of bioprinted structures ($p < 0.05$). (c) F-actin/DAPI staining of fibroblast embedded in the 3D bioprinted structures with GelMA and GelMA-PEGDA at days 1, 3, and 7 (Scale bar = 100 μm).

intensity increased, likely due to variations in material stiffness. For GelMA inks, no significant differences were observed between treatments on days 1 and 3. In contrast, for GelMA-PEGDA, statistical differences in aspect ratio were noted between groups 1 and 4 ($p < 0.05$). Over time, the differences in cell morphology due to light intensity diminished, with the cells forming networks. These differences in morphology between GelMA and GelMA-PEGDA may be associated with the lower disponibility of RGD peptides and the polymer network's density, as well the stiffness of these materials may influence cell mechanosensing and proliferation [2, 64–67].

Cell density was analyzed by counting the number of 3T3 cells within the entire structure, which comprised four distinct regions, and then normalizing the average cell count in each region. This analysis was performed for both GelMA and GelMA-PEGDA bioinks. On day 1, GelMA showed similar cell densities across all regions, indicating a homogeneous distribution of cells (figure 6(i)). This trend continued on day 3, with an overall threefold increase in cell density compared to day 1. By day 7, significant statistical differences in cell density were observed between region 1 and regions 2, 3, and 4, reflecting a pattern similar to that seen in the metabolic activity assay. For the GelMA-PEGDA samples (figure 6(k)), no significant differences in cell density were noted between regions on day 1. However, by day 7, statistically significant differences in cell density between region 1 and region 4 became apparent, mirroring the trend observed in the GelMA samples. Although there were slight differences in metabolic activity and cell density between region 1 and regions 2, 3, and 4, all samples remained viable and proliferated throughout the experimental period. Notably, the differences were primarily confined to region 1, while the other three regions exhibited similar behavior. This contrasts with the exposure time experiments, where significant differences were observed across all three exposure times. These findings align with the results of Bhanvadia *et al*, where regions exposed to shorter crosslinking times demonstrated higher cell viability [49], confirming our observation

that exposure time has a greater impact on cell viability than laser intensity.

4.7. Bioprinting of bronchial-like structures via segmentation technique

The previous characterization suggests that a short exposure time with higher intensity is more cell-friendly than a longer exposure time with lower energy. When combined with the segmentation process, this approach could facilitate the bioprinting of structures with higher cell viability. In our biofabrication process using laser-based DLP, we utilized an intensity of 0.1105 mW mm^{-2}, which enables higher resolution and faster crosslinking but also supports better cell viability. With our robust biofabrication process using laser-based DLP, we tested the bioprinting of a bronchial branch using the segmentation technique with both bioinks (GelMA and GelMA PEGDA) (figure 7). The live-dead assay shows an increase in the number of cells and sustained cell viability of up to 90% for GelMA and up to 85% for GelMA PEGDA bioprinted constructs across seven days with statistical differences between bioinks ($p < 0.05$) (figures 7(a) and (b)). Nonetheless, the fluorescent micrographs reveal the fibroblast morphology within the bioink matrix. These results were confirmed by using the phalloidin staining, where, on day 7, it is observable that the GelMA sample displays cytoskeletal development and spreading, indicating possible cell migration and growth. In contrast, the GelMA-PEGDA sample shows less spreading, suggesting that the incorporation of GelMA may be more supportive of cell migration and structural organization (figure 7(c)).

5. Conclusion

This study presents a comprehensive analysis of the transition from LED-based to laser-based light sources in DLP bioprinting systems, highlighting the advantages of laser systems in enhancing resolution, reducing printing time, and improving dynamic range. By leveraging the higher power, spectral precision, and favorable étendue characteristics of

laser sources, the proposed dual-laser DLP system has been shown to address the inherent limitations of LED systems. Specifically, the system delivered a two-fold increase in resolution and a twelvefold reduction in printing time, significantly enhancing the efficiency and quality of printed biostructures. Our findings emphasize the critical impact of exposure time and laser intensity on cell viability. Shorter exposure times at higher laser intensities proved to be more cell-friendly, resulting in better recovery, higher metabolic activity, and cell viability over time, with higher aspect ratios and cell density. The effect of these parameters stems from two key aspects: first, the toxicity of light exposure to cells, where prolonged exposure has been reported to induce DNA mutations and ROS production; and second, the density of the hydrogel cross-linking network, which influences hydrogel stiffness and structural integrity. Both aspects have been reported to directly affect cell proliferation and metabolic pathways. These aspects were carefully balanced using the adaptive segmentation control method, which minimized over-crosslinking while maintaining the resolution required for complex structures. This method enabled the bioprinting of intricate, anatomically relevant structures, such as the bronchi model with a 14.43x compression ratio, demonstrating minimal error and sustained cell viability. The enhanced capabilities of the laser system, combined with the innovative segmentation technique, open new possibilities for the bioprinting of complex and intricate structures with high precision and biological relevance. The improvements in resolution, dynamic range, and printing speed, combined with enhanced material compatibility and cell-friendly processes, position the dual-laser DLP system as a promising technology for advancing the field of 3D bioprinting. This work not only advances the field of 3D bioprinting but also sets a foundation for future developments in biofabrication technologies, paving the way for more sophisticated and efficient biomedical applications.

Data availability statement

All data that support the findings of this study are included within the article (and any supplementary files).

Acknowledgment

ORCID iDs

Jorge Alfonso Tavares-Negrete ⓘ
https://orcid.org/0000-0001-7695-460X
Rahim Esfandyarpour ⓘ https://orcid.org/0000-0002-4528-3601
Ozdal Boyraz ⓘ https://orcid.org/0000-0002-4005-1107

References

[1] Bhusal A, Dogan E, Nguyen H-A, Labutina O, Nieto D, Khademhosseini A and Miri A K 2021 Multi-material digital light processing bioprinting of hydrogel-based microfluidic chips *Biofabrication* **14** 014103

[2] Tavares-Negrete J A, Babayigit C, Najafikoshnoo S, Lee S W, Boyraz O and Esfandyarpour R 2023 A novel 3D-bioprinting technology of orderly extruded multi-materials via photopolymerization *Adv. Mater. Technol.* **8** 2201926

[3] Lakshminarayanan A and Richuso J 2024 The next generation of DLP Pico technology for augmented reality (AR) displays," in optical architectures for displays and sensing in augmented, virtual, and mixed reality (AR, VR, MR) V *Proc. SPIE* **12913** 141–9

[4] Meza J, Contreras-Ortiz S H, Perez L A R and Marrugo A G 2021 Three-dimensional multimodal medical imaging system based on freehand ultrasound and structured light *Opt. Eng.* **60** 054106

[5] Kalyoncu S K, Torun R, Huang Y, Zhao Q and Boyraz O 2014 Fast dispersive laser scanner by using digital micro mirror arrays *J. Micro Nano-Manuf.* **2** 021004

[6] Kalyoncu S K, Huang Y, Song Q and Boyraz O 2012 Analytical study on arbitrary waveform generation by MEMS micro mirror arrays *Opt. Express* **20** 27542–53

[7] Grigoryan B *et al* 2019 Multivascular networks and functional intravascular topologies within biocompatible hydrogels *Science* **364** 458–64

[8] Grix T, Ruppelt A, Thomas A, Amler A-K, Noichl B, Lauster R and Kloke L 2018 Bioprinting perfusion-enabled liver equivalents for advanced organ-on-a-chip applications *Genes* **9** 4

[9] Kalyoncu S K, Huang Y, Song Q and Boyraz O 2013 Fast arbitrary waveform generation by using digital micromirror arrays *IEEE Photonics J.* **5** 5500207

[10] Yang W, Yu H, Liang W, Wang Y and Liu L 2015 Rapid fabrication of hydrogel microstructures using UV-induced projection printing *Micromachines* **6** 12

[11] Yang W, Cai S, Chen Y, Liang W, Lai Y, Yu H, Wang Y and Liu L 2020 Modular and customized fabrication of 3D functional microgels for bottom-up tissue engineering and drug screening *Adv. Mater. Technol.* **5** 1900847

[12] Zhang J, Hu Q, Wang S, Tao J and Gou M 2019 Digital light processing based three-dimensional printing for medical applications *Int. J. Bioprinting* **6** 242

[13] Chiulan I, Heggset E B, Voicu Ş I and Chinga-Carrasco G 2021 Photopolymerization of bio-based polymers in a biomedical engineering perspective *Biomacromolecules* **22** 1795–814

[14] Lee J *et al* 2022 Average-accumulated normalized dose (A-AND) predicts ultimate tensile strength and elastic modulus of photopolymer printed by vat photopolymerization *Addit. Manuf.* **55** 102799

[15] Xu H-Q, Liu J-C, Zhang Z-Y and Xu C-X 2022 A review on cell damage, viability, and functionality during 3D bioprinting *Mil. Med. Res.* **9** 70

[16] Janssens P and Malfait K 2009 Future prospects of high-end laser projectors," in emerging liquid crystal technologies IV *Proc. SPIE* **7232** 247–58

[17] Loterie D, Delrot P and Moser C 2020 High-resolution tomographic volumetric additive manufacturing *Nat. Commun.* **11** 852

[18] Kim M M and Darafsheh A 2020 Light sources and dosimetry techniques for photodynamic therapy *Photochem. Photobiol.* **96** 280–94

[19] Das P, Najafikhoshnoo S, Tavares-Negrete J A, Yi Q and Esfandyarpour R 2022 An *in-vivo*-mimicking 3D lung cancer-on-a-chip model to study the effect of external stimulus on the progress and inhibition of cancer metastasis *Bioprinting* **28** e00243

[20] Chen Y *et al* 2020 Noninvasive *in vivo* 3D bioprinting *Sci. Adv.* **6** eaba7406

[21] Toombs J T, Luitz M, Cook C C, Jenne S, Li C C, Rapp B E, Kotz-Helmer F and Taylor H K 2022 Volumetric additive manufacturing of silica glass with microscale computed axial lithography *Science* **376** 308–12

[22] Tavares-Negrete J A, Pedroza-González S C, Frías-Sánchez A I, Salas-Ramírez M L, de Santiago-miramontes M D L Á, Luna-Aguirre C M, Alvarez M M and Trujillo-de Santiago G 2023 Supplementation of GelMA with minimally processed tissue promotes the formation of densely packed skeletal-muscle-like tissues *ACS Biomater. Sci. Eng.* **9** 3462–75

[23] Yzuel M J 1999 Image formation and optical transfer function in a course of fourier optics *Education and Training in Optics and Photonics (1999), paper EPOP147* (Optica Publishing Group) p EPOP147 (available at: https://opg.optica.org/abstract.cfm?uri=ETOP-1999-EPOP147) (Accessed 27 June 2024)

[24] Garciamendez-Mijares C E *et al* 2024 Design considerations for digital light processing bioprinters *Appl. Phys. Rev.* **11** 031314

[25] Field J J, Squier J A and Bartels R A 2019 Fluorescent coherent diffractive imaging with accelerating light sheets *Opt. Express* **27** 13015–30

[26] Williams T 2017 *The Optical Transfer Function of Imaging Systems* (Routledge) (https://doi.org/10.1201/9780203736296)

[27] Deng Y and Chu D 2017 Coherence properties of different light sources and their effect on the image sharpness and speckle of holographic displays *Sci. Rep.* **7** 5893

[28] Piotrowski J J, Vorobiev D, Robberto M and Smee S A 2022 Optical diffraction simulation of a digital micromirror device," in emerging digital micromirror device based systems and applications XIV *Proc. SPIE* **12014** 45–52

[29] Higley D J, Winters D G, Futia G L and Bartels R A 2012 Theory of diffraction effects in spatial frequency-modulated imaging *J. Opt. Soc. Am.* A **29** 2579–90

[30] Gross H 2005 *Handbook of Optical Systems, Volume 1, Fundamentals of Technical Optics* vol 1 (Wiley) (available at: https://ui.adsabs.harvard.edu/abs/2005hosv.book.....G) (Accessed 7 July 2024)

[31] Christensen R 2005 Speckle reduction for ultrahigh resolution laser projectors

[32] Edgar M P, Gibson G M and Padgett M J 2019 Principles and prospects for single-pixel imaging *Nat. Photon.* **13** 13–20

[33] Hellman B 2021 Novel DMD-based lidar and display systems *PhD* The University of Arizona, United States—Arizona (available at: www.proquest.com/docview/2533295055/abstract/117A232D5B4E447FPQ/1) (Accessed 7 July 2024)

[34] (DLP5500 data sheet, product information and support | TI.com) (available at: www.ti.com/product/DLP5500?bm-verify=AAQAAAAJ_____9W_l3O67vgQKduuqmWzMJ1kcpH9SZca9A5dqP8RKNrOYs9cAOcs4un7MKSMPp3ykUpialZfXUjUI2FI3NmWBzRpj2BLCi-KVkT_CXfKQQREwCfx4JwYeI3EFazGXsqi2hBZANzDUGoPAP6-DFEC08O-dgAy9TOV-ytuC16Z9WH-ux-vilTZ7JEiuTZCCYNQXPUCm7hTXEMW8_eGIYbkK4S80vt4go48CxAQzmNslkq6l3138mi917N2M2u-YNVJ_VkKETGbUk00FM4MvYPLo0Gkt733A4KA5BuviQWeG5gUe2LY) (Accessed 7 July 2024)

[35] Rong L, Xiao W, Pan F, Liu S and Li R 2010 Speckle noise reduction in digital holography by use of multiple polarization holograms *Chin. Opt. Lett.* **8** 653–5

[36] Nomura T, Okamura M, Nitanai E and Numata T 2008 Image quality improvement of digital holography by superposition of reconstructed images obtained by multiple wavelengths *Appl. Opt.* **47** D38–D43

[37] Su T-W, Isikman S O, Bishara W, Tseng D, Erlinger A and Ozcan A 2010 Multi-angle lensless digital holography for depth resolved imaging on a chip *Opt. Express* **18** 9690–711

[38] Kubota S and Goodman J W 2010 Very efficient speckle contrast reduction realized by moving diffuser device *Appl. Opt.* **49** 4385–91

[39] Li N-N, Chen C, Lee B, Wang D and Wang Q-H 2022 Speckle noise suppression algorithm of holographic display based on spatial light modulator *Front. Photon.* **2** 825610

[40] Jenkins E L and Burrell D J 2023 Improved active-tracking performance through Hadamard speckle contrast reduction *Opt. Lett.* **48** 5515–8

[41] Chellappan K V, Erden E and Urey H 2010 Laser-based displays: a review *Appl. Opt.* **49** F79–F98

[42] Montgomery S M, Hamel C M, Skovran J and Qi H J 2022 A reaction–diffusion model for grayscale digital light processing 3D printing *Extrem. Mech. Lett.* **53** 101714

[43] Dileep C, Jacob L Umer R and Butt H 2024 Review of vat photopolymerization 3D printing of photonic devices *Addit. Manuf.* **86** 104189

[44] Ashfaq A, Clochard M-C, Coqueret X, Dispenza C, Driscoll M S, Ulański P and Al-Sheikhly M 2020 Polymerization reactions and modifications of polymers by ionizing radiation *Polymers* **12** 2877

[45] Liang J, Francoeur M, Williams C B and Raeymaekers B 2023 Curing characteristics of a photopolymer resin with dispersed glass microspheres in vat polymerization 3D printing *ACS Appl. Polym. Mater.* **5** 9017–26

[46] Ligon S C, Liska R, Stampfl J, Gurr M and Mülhaupt R 2017 Polymers for 3D printing and customized additive manufacturing *Chem. Rev.* **117** 10212–90

[47] Luu T T H, Jia Z, Kanaev A and Museur L 2020 Effect of light intensity on the free-radical photopolymerization kinetics of 2-Hydroxyethyl methacrylate: experiments and simulations *J. Phys. Chem.* B **124** 6857–66

[48] He N *et al* 2023 Photoinhibiting via simultaneous photoabsorption and free-radical reaction for high-fidelity light-based bioprinting *Nat. Commun.* **14** 3063

[49] Bhanvadia A A, Farley R T, Noh Y and Nishida T 2023 3D printing of hollow geometries using blocking liquid substitution stereolithography *Sci. Rep.* **13** 434

[50] You S, Wang P, Schimelman J, Hwang H H and Chen S 2019 High-fidelity 3D printing using flashing photopolymerization *Addit. Manuf.* **30** 100834

[51] Polat S, Öksüzler M, Öksüzler F Y, Özsahin E and Göker P 2023 Radiological and anatomical evaluation of the tracheal morphology and morphometry in Turkish adults *Int. J. Morphol.* **41** 1625–30

[52] Wang Z, Jin X, Dai R, Holzman J F and Kim K 2016 An ultrafast hydrogel photocrosslinking method for direct laser bioprinting *RSC Adv.* **6** 21099–104

[53] Anupama Sekar J, Velayudhan S and Anil Kumar P R 2023 Biocompatibility evaluation of antioxidant cocktail loaded gelatin methacrylamide as bioink for extrusion-based 3D bioprinting *Biomed. Mater.* **18** 044101

[54] Noshadi I *et al* 2017 *In vitro* and *in vivo* analysis of visible light crosslinkable gelatin methacryloyl (GelMA) hydrogels *Biomater. Sci.* **5** 2093–105

[55] Jia W *et al* 2016 Direct 3D bioprinting of perfusable vascular constructs using a blend bioink *Biomaterials* **106** 58–68

[56] Ladoux B and Mège R-M 2017 Mechanobiology of collective cell behaviours *Nat. Rev. Mol. Cell Biol.* **18** 743–57

[57] Butenko S *et al* 2024 Hydrogel crosslinking modulates macrophages, fibroblasts, and their communication, during wound healing *Nat. Commun.* **15** 6820

[58] Dupont S *et al* 2011 Role of YAP/TAZ in mechanotransduction *Nature* **474** 179–83

[59] Chakraborty M *et al* 2021 Mechanical stiffness controls dendritic cell metabolism and function *Cell Rep.* **34** 108609

[60] Romani P *et al* 2024 Mitochondrial mechanotransduction through MIEF1 coordinates the nuclear response to forces *Nat. Cell Biol.* **26** 2046–60

[61] Na J, Yang Z, Shi Q, Li C, Liu Y, Song Y, Li X, Zheng L and Fan Y 2024 Extracellular matrix stiffness as an energy metabolism regulator drives osteogenic differentiation in mesenchymal stem cells *Bioact. Mater.* **35** 549–63

[62] Piluso S, Skvortsov G A, Altunbek M, Afghah F, Khani N, Koç B and Patterson J 2021 3D bioprinting of molecularly engineered PEG-based hydrogels utilizing gelatin fragments *Biofabrication* **13** 045008

[63] Lin R-Z, Chen Y-C, Moreno-Luna R, Khademhosseini A and Melero-Martin J M 2013 Transdermal regulation of vascular network bioengineering using a photopolymerizable methacrylated gelatin hydrogel *Biomaterials* **34** 6785–96

[64] Wang Z, Abdulla R, Parker B, Samanipour R, Ghosh S and Kim K 2015 A simple and high-resolution stereolithography-based 3D bioprinting system using visible light crosslinkable bioinks *Biofabrication* **7** 045009

[65] Babayigit C, Tavares-Negrete J A, Najafikhoshnoo S, Esfandyarpour R and Boyraz O 2024 Advancing 3D-bioprinting with photopolymerization of orderly extruded multimaterials (POEM)," in laser 3D manufacturing XI *Proc. SPIE* **12876** 9–13

[66] Tavares Negrete J A *et al* Impact of exposure time and power intensity on cell viability in 3D bioprinting *Laser 3D Manufacturing XII*

[67] Babayigit C, Alfonso Tavares-Negrete J, Esfandyarpour R and Boyraz O 2024 Segmentation approach for enhanced DLP bioprinting in laser 3D manufacturing XII *Proc. SPIE* (available at: https://spie.org/photonics-west/presentation/Segmentation-approach-for-enhanced-DLP-bioprinting/13354-40) accepted